Ni-doping-induced oxygen vacancy in Pt-CeO$_2$ catalyst for toluene oxidation: Enhanced catalytic activity, water-resistance, and SO$_2$-tolerance

Menglan Xiao [a,e], Dawei Han [b], Xueqin Yang [c], Narcisse Tsona Tchinda [d], Lin Du [d], Yucong Guo [a], Yuechang Wei [b], Xiaolin Yu [a,*], Maofa Ge [a,e]

[a] State Key Laboratory for Structural Chemistry of Unstable and Stable Species, Beijing National Laboratory for Molecular Sciences (BNLMS), CAS Research/Education Center for Excellence in Molecular Sciences, Institute of Chemistry, Chinese Academy of Sciences, Beijing 100190, PR China
[b] State Key Laboratory of Heavy Oil Processing, China University of Petroleum, Beijing 102249, PR China
[c] College of Forestry, Henan Agricultural University, Zhengzhou 450002, PR China
[d] Environment Research Institute, Shandong University, Qingdao 266237, PR China
[e] University of Chinese Academy of Sciences, Beijing 100049, PR China

ARTICLE INFO

ABSTRACT

It is a challenge to enhance the catalytic activity of the oxidation of volatile organic compounds (VOCs) and the poison-tolerance capacity in the practical application. Here, we report the construction of Pt/Ni-CeO$_2$ catalyst via Ni doping, which exhibited the excellent toluene catalytic performance, as well as remarkably improved water-resistance and SO$_2$-tolerance. The electron energy loss spectroscopy and density functional theory calculations demonstrated that the doped Ni species induced the generation of abundant oxygen vacancies from bulk to the surface, improving the redox property, activation of oxygen species, and adsorption capacity of toluene molecules. Moreover, the Pt-NiO interfacial structure was formed by the thermal-driven Ni species to the adjacent Pt species, which could modify the electronic and chemical properties of Pt, thus restraining the adsorption of water and SO$_2$ molecules. This investigation provides new insights into the activation of oxygen species via oxygen vacancies, and anti-poison activity via surface modification engineering for catalyst development in practical applications.

1. Introduction

Volatile organic compounds (VOCs), such as benzene, toluene, and xylenes (BTX), mainly generated from the petrochemical industry, are harmful to human health and the atmospheric environment [1–3]. In recent years, great efforts have been applied to the control engineering of VOCs emissions. Kinds of technologies, including absorption, membrane separation, biological treatment, photocatalytic removal, and catalytic oxidation, have achieved a certain effect on the degradation of VOCs [4]. Among them, catalytic oxidation is regarded as a promising method, due to its high efficiency, energy saving quality, and environmental friendliness [5,6]. The noble metal materials present an excellent catalytic performance for VOCs abatement at low temperature, but their easy sintering at high temperature and poisoning in real working conditions restrict their practical application in VOCs elimination [7]. Thus, the rational design of high-efficiency and practical-used catalysts for VOCs degradation still has a great demand.

As is well known that for noble metal catalysts, the presence of H$_2$O can form the less active M-(OH)$_x$ or block the active centers, and SO$_2$ results in the formation of the irreversible M-SO$_4$ species. In general, the electron transfer will occur between noble metals and SO$_2$ or water molecule to reduce the electron cloud density of the d-orbital, restraining the adsorption and activation of reactant molecules [8]. The surface decoration of the metal oxide could adjust the electronic properties of the noble metal surface by changing the d-orbital overlap to influence the dissociative adsorption energies of small molecules [9]. For example, the strong electronic interaction between Pt and M (Fe, Co, Ni) not only improved the replenished capacity of oxygen, but also weakened the adsorption ability, so as to remain stable for CO oxidation in the presence of water [10]. WO$_x$ decorated on Pt/CeO$_2$ catalyst was conducive to the formation of W-O-Ce and Pt-O-W bonds, of which the Pt atom cannot interact with charged species, such as oxygen atoms in water, due to charge transfer from W to Pt, thus guaranteeing a good stability in the wet feed [11]. Furthermore, the addition of V in

$Fe_\delta Ce_{1-\delta}VO_4$ catalysts led to an interaction between V and Fe species, and the V species might prefer to gain electrons from Fe species, which was conducive to the increase of the amount of Lewis acids and the effective suppression of SO_2 adsorption [12]. Xu et al. reported that an electronic transfer between Cu cations and V cations in $10Cu-3V/\gamma-Al_2O_3$ benefited to the formation of more surface chemical oxygen and suppressed the generation of sulfates on catalyst surface, which contributed to the excellent sulfur resistance for VOCs removal [13]. The synergistic effect of Pt and Ni in $Pt-Ni/CeO_2$ catalyst also promoted the anti-coke property during the reforming reaction [14,15]. Nevertheless, the adverse influence is that the surface decoration of transition metal oxide may inevitably override some active sites to restrain the activation of oxygen molecules.

The activation of molecular oxygen is a critical factor for catalytic oxidation, which could guide the synthesis of catalysts [16]. Generally, the chemically inert O_2 molecule is difficultly activated unless under high temperature and pressure. Abundant defects, especially surface oxygen vacancies, provide a feasible route to lower the associated barriers for O_2 molecule activation by electron transfer into antibonding orbitals [17]. CeO_2 owns the unique oxygen storage capacity, redox properties, and defect structure, which are suitable for O_2 activation. Moreover, the doping of a secondary metal cation in the CeO_2 lattice could induce the formation of more oxygen vacancies to further promote the ability of O_2 activation. The isotopic oxygen studies have proven that lattice oxygen atom (^{16}O) was easily released to generate oxygen vacancy after Pr and La doping in CeO_2 [18]. Moreover, the Y-doped CeO_2 not only increased the number of oxygen vacancies, but also enhanced the metal−support interaction [19]. Compared with rare-earth ions, the doping of transition metal ions (Mn, Fe, Co, Ni, et al.) into CeO_2 lattice had a remarkable influence on Ce coordination shell, resulting in the formation of longer Ce-O bonds to promote the oxygen storage capacity of the solid solution [20,21]. However, doping CeO_2 with single metal ions was insufficient to meet the demands of low-temperature activity. In most case, the high catalytic activity could be achieved through the synergistic effect in multicomponent system by changing the electronic state or geometry of the active sites [22]. Xu et al. reported that Cr^{3+} doping in Ru/CeO_2 could facilitate the formation of surface oxygen vacancies and hydroxyl groups, thus increasing the amount of bicarbonates and formates in low-temperature CO_2 methanation [23]. Emiel et al. confirmed that the oxygen vacancy derived from Fe doping in Pt/CeO_2 catalysts accelerated the N_2O decomposition to solve the root problem of limited N_2 selectivity at low temperature [24]. These inspire us to construct abundant oxygen vacancies by adding secondary metal cations to enhance the catalytic activity. Therefore, it is warranted to find a balanced method, which not only creates plentiful oxygen vacancies, but also improves the water-resistance and SO_2-tolerance performance.

Herein, we report a strategy to fabricate a superior $Pt/Ni-CeO_2$ catalyst via doping Ni for toluene oxidation. The $Pt/Ni-CeO_2$ catalyst exhibited high toluene conversion, excellent water-resistance, and SO_2-tolerance. The X-ray diffraction (XRD) patterns, electron energy loss spectroscopy (EELS), and density functional theory (DFT) calculations demonstrated that the Ni species were doped into the CeO_2 lattice to form abundant oxygen vacancies from bulk to the surface of catalyst. The surface oxygen vacancies contributed to the activation of gaseous oxygen and the bulk oxygen vacancies were conducive to the migration ability of lattice oxygen, all which promoted the participation of oxygen species in the toluene catalytic oxidation reaction. Meanwhile, the annealing drove partial Ni species to the catalyst surface adjacent to Pt species, which formed the Pt-NiO interfacial structure to modify the electronic and chemical properties of Pt species, thus restraining the adsorption of water and SO_2 molecules. As a contrast, the $Pt-Ni/CeO_2$ catalyst would override the surface oxygen vacancies, thus weakening the adsorption and activation ability, but slightly improving water-resistance and SO_2-tolerance. The roles of surface and bulk oxygen vacancies in catalytic degradation mechanism were well investigated.

2. Experimental

2.1. Synthesis of supports and catalysts

2.1.1. Synthesis of CeO_2

The CeO_2 sample was prepared through a hydrothermal method [25]. To be more specific, 5 g of $Ce(NO_3)_3 \cdot 6H_2O$ was dissolved in a mixed solution including 5 mL of deionized water and 5 mL of propionic acid for 30 min 90 mL of ethylene glycol was added to the above solution that kept stirring for 2 h. Then, the solution was transferred into a Teflon-lined stainless-steel autoclave and heated at 160 °C for 8 h. After cooling to room temperature, the precipitates were collected by centrifugation, washed with deionized water and ethanol three times, and then dried under vacuum at 60 °C overnight. The CeO_2 sample was obtained after calcinating the precipitates at 600 °C for 6 h in air.

2.1.2. Synthesis of $Ni-CeO_2$

The synthesis process of Ni-doping sample named as $Ni-CeO_2$ was similar to the preparation of CeO_2. 491.0 mg of $Ni(NO_3)_2 \cdot 6H_2O$ was added into the mixed solution, and treated hydrothermally. Then, the following procedures were same was as above.

2.1.3. Synthesis of Pt/CeO_2

The Pt/CeO_2 sample was prepared by a $NaBH_4$ reduced method. 1.44 mL of $PtCl_4$ aqueous solution (3.47 mg/mL) was added in 40 mL of deionized water. 500 mg of CeO_2 powder was dispersed into the above solution and the mixture was stirred for 1 h. 9.7 mg of $NaBH_4$ was added into the suspension under stirring for 2 h. The sample was collected and washed with deionized water by centrifugation, and dried in a vacuum oven at 60 °C. Finally, the Pt/CeO_2 sample was annealed at 500 °C for 2 h in air.

2.1.4. Synthesis of $Pt/Ni-CeO_2$

The $Pt/Ni-CeO_2$ sample was prepared the same way as that mentioned above except that 525.0 mg of $Ni-CeO_2$ were used as supports.

2.1.5. Synthesis of $Pt-Ni/CeO_2$

Similarly, the $Pt-Ni/CeO_2$ sample employed $PtCl_4$ and $Ni(NO_3)_2 \cdot 6H_2O$ as metal precursor to support on CeO_2. In brief, 1.44 mL of $PtCl_4$ aqueous solution (3.47 mg/mL) and 123.9 mg of $Ni(NO_3)_2 \cdot 6H_2O$ were dissolved in 40 mL of deionized water. 500 mg of CeO_2 powder was dispersed, and then stirred for 1 h. Thereafter, 9.7 mg of $NaBH_4$ was added into the suspension under stirring for 2 h. The sample was collected, washed and dried. The $Pt-Ni/CeO_2$ sample was obtained by calcining at 500 °C for 2 h in air.

2.2. Characterization

The morphology of the catalysts was characterized by transmission electron microscopy (TEM), scanning electron microscopy (SEM), frozen electron microscopy, and high-resolution transmission electron microscopy (HRTEM). The physicochemical properties of the catalysts were investigated by N_2 adsorption-desorption isotherms (BET), X-ray diffraction (XRD) patterns, Raman spectra, H_2 temperature programmed reduction (H_2-TPR), O_2 temperature programmed desorption (O_2-TPD), CO chemisorption, toluene temperature programmed desorption, oxygen multi-pulse experiment, X-ray photoelectron spectroscope (XPS), X-ray absorption spectroscopy (XAS) and in situ diffuse reflectance infrared fourier transform spectroscopy (in situ DRIFT). The experiment details are given in the Supporting Information (SI).

2.3. Catalytic activity test

The toluene combustion of as-prepared catalysts was evaluated in a continuous flow fixed-bed reactor. The specific test conditions are

described in the Supporting Information.

3. Results and discussion

3.1. Structure and morphological properties of catalysts

Fig. 1 exhibit the XRD patterns of the catalysts and corresponding supports. The diffraction peaks of all samples in Fig. 1a could be indexed to the face-centered cubic fluorite structure of CeO_2, and no peaks of Ni-related species and Pt species were observed. However, the peak of (111) facet exhibited an obvious difference. As shown in Fig. 1b, Pt/CeO_2 and Pt-Ni/CeO_2 samples exhibited the similar (111) peak values with the CeO_2 sample, while the peak of (111) facet in Ni-CeO_2 and Pt/Ni-CeO_2 samples was shifted to a slightly high 2θ value, indicating that Ni was successfully doped into the ceria lattice structure. Generally, if Ni species was doped into CeO_2 to replace Ce^{4+} without other effects, the 2θ values should remarkably increase together with the significant decrease of lattice parameter due to the discrepancy in coordination number and ionic radius. Table 1 showed that the decrease of lattice parameter in Pt/Ni-CeO_2 sample was slight, implying the occurrence of compensation for the lattice shrink. That is, the incorporation of Ni^{2+} (0.69 Å) would induce the formation of more Ce^{3+} with a larger ionic radius (1.02 Å) to compensate for the lattice shrink effect compared with that of Ce^{4+} (0.87 Å) [23]. Therefore, the slight shrink of CeO_2 lattice in the Pt/Ni-CeO_2 sample reflected the formation of more bulk defect sites and vacancies.

The morphologies and microstructures of as-prepared samples were studied by SEM and TEM. Ni-CeO_2, Pt/Ni-CeO_2, Pt/CeO_2, and Pt-Ni/CeO_2 samples displayed a homogeneous nanosphere with litchi-like rough surface, which are the same as the CeO_2 sample (Fig. S1 and Fig. S2). The doping of Ni species in Ni-CeO_2 and Pt/Ni-CeO_2 leads to the reduction of CeO_2 crystal size and nanosphere size (Fig. 2a and Fig. 2b). The detailed description is given in SI. As shown in Fig. S4, the (111) and (220) facets of CeO_2 with the lattice spacings of ca. 0.312 and 0.191 nm were clearly seen in CeO_2 and Ni-CeO_2 supports. No obvious Ni species was observed in the Ni-CeO_2 sample. The HRTEM image of Pt/Ni-CeO_2 in Fig. 2c also revealed the (111) and (220) facet of CeO_2. The interplanar spacing of 0.226 nm belonging to Pt (111) demonstrated the presence of metallic Pt nanoparticles. Surprisingly, some NiO nanoparticles with lattice spacing of 0.208 nm adjacent to Pt species were observed, which may be attributed to the surface Ni species segregation induced by the annealing. HADDF-STEM and the corresponding elemental mappings images (Fig. S5) verified that Ni species appeared in the vicinity of Pt species, besides the existence in the ceria lattice structure. According to previous reports, the high temperature played a critical role in the metastable subsurface Ni atom segregation to form the stable NiO species on the catalyst surface [26]. Meanwhile, the segregation phenomenon arose from the adsorbate-dependent modification

of the electronic structure of the surface [27]. Thus, the Ni atoms diffused from the CeO_2 were inclined to depositing adjacent to the Pt species, which was beneficial to the formation of Pt-NiO interfacial structure. Thus, it could be deduced that there was an electronic interaction between Pt and NiO. The elemental mapping results in Fig. 2d represent a good distribution of Pt and Ni species in the entire region. HRTEM images in Fig. S6 showed that Pt/CeO_2 and Pt-Ni/CeO_2 samples also exposed the dominated CeO_2 (111), (200), (220) planes, and Pt (111) planes. Meanwhile, small NiO nanoparticles adjacent to Pt species (Fig. S6b) were also observed besides individual NiO nanoparticles in the Pt-Ni/CeO_2 sample (Fig. S6c).

X-ray absorption fine structure (XAFS) is used to further analyze the local structure of the samples in depth. The Fourier-transformed k^2-weighted $\chi(k)$ spectra at Ce L$_3$-edge spectra (EXAFS) are shown in Fig. 3a. The maximum peak at 1.8 Å was assigned to the scattering effect of neighboring O atoms (Ce–O bond, first shell), and the peak at 3.5 Å was attributed to the nearest coordination of Ce atoms (Ce–Ce bond, second shell) [28]. The Pt/Ni-CeO_2 sample exhibited a relatively weaker intensity of Ce-O peak than the Pt/CeO_2 sample, followed by the Pt-Ni/CeO_2 sample, indicating the low coordination number and high concentration of the oxygen vacancy in the Pt/Ni-CeO_2 sample [29]. Meanwhile, the slightly positive shift of the Ce-O bond in the Pt/Ni-CeO_2 sample signified a stretched bond length, which would facilitate the weakening of the Ce-O bond to release the lattice oxygen. For the second shell, the Ce-Ce scattering distance in the Pt/Ni-CeO_2 sample was slightly reduced compared with other two samples, proving that the Ni atom replaced the Ce atom to form a short Ce-Ni bond. Ni K-edge EXAFS spectra in Fig. 3b show that the lengths of the Ni-O bond and Ni-Ni bond in the NiO standard sample were 1.6 and 2.4 Å, respectively [30]. The Ni-Ni scattering peak in Pt-Ni/CeO_2 shifted to a high distance, probably because some Ni atoms linked to Pt atoms to generate Ni-Pt bonds. Pt L$_3$-edge EXAFS spectra in Fig. S7 also confirmed the existence of Ni-Pt bonds, which evidenced the modification of Pt by Ni species on the surface of the catalyst. The coordination number of Ni-Ni bond decreased in Pt/Ni-CeO_2 sample according to the peak intensity, manifesting that some Ni atoms was segregated from the bulk Ni species to bond with Pt atoms [31]. Meanwhile, the Pt/Ni-CeO_2 sample exhibited a higher R value of Ni-Ni bond than Pt-Ni/CeO_2, but lower than Ni-CeO_2 (Fig. 3b) due to the formation of numerous Ni-Ce bonds in Ni-CeO_2, further confirmed the formation of Ni-Pt bonds besides Ni-Ce bonds. These results provide direct evidence of Pt-NiO interfacial structure formation in Pt-Ni/CeO_2 and Pt/Ni-CeO_2 samples. In the Pt-NiO interface, the surface d-band structure of Pt species would be influenced by Ni species, causing the changes in the electronic and chemical properties [9,10].

3.2. Surface property

Raman was conducted to investigate the lattice distortion of as-prepared samples. In Fig. 4a, a strong peak at 467 cm^{-1} in Raman spectra was assigned to the F_{2g} vibration mode of CeO_2 in a cubic fluorite structure. It is worth noting that two new peaks at 559 and 623 cm^{-1} appeared in Ni-CeO_2 and Pt/Ni-CeO_2 samples, corresponding to surface oxygen vacancies, where Ce^{4+} was replaced by Ce^{3+} (D$_1$) and the intrinsic defect in ceria (D$_2$), respectively [32]. Due to the doping of Ni

Table 1
Physicochemical Properties of the Samples.

| Sample	Lattice parameter (Å)	O_{ads}/O_{total} (%)	Pt^0/Pt_{total} (%)	Ce^{3+}/Ce_{total} (%)
Pt-Ni/CeO_2	5.394	36.2	15.4	15.9
Pt/CeO_2	5.402	22.0	18.6	17.3
Pt/Ni-CeO_2	5.376	40.5	22.9	19.1
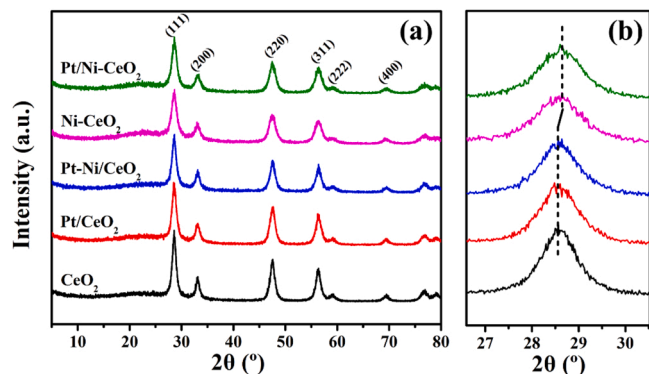
**Fig. 1.** XRD patterns of all samples. (a) complete profiles; (b) partially enlarged profiles.
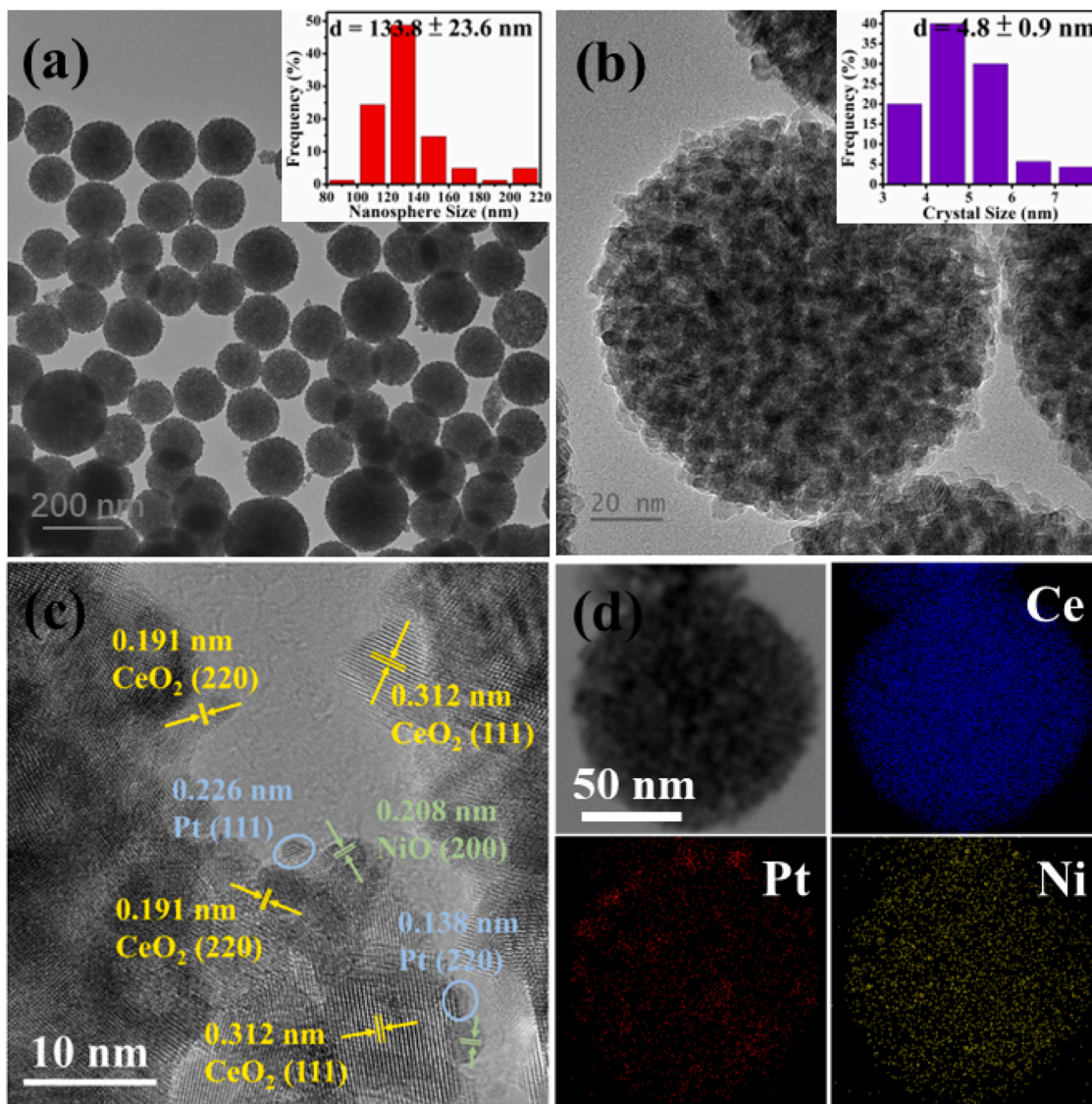
Fig. 2. (a) TEM image and the frequency distribution of CeO_2 nanosphere in Pt/Ni-CeO_2; (b) HRTEM image and the frequency distribution of CeO_2 crystal particle in Pt/Ni-CeO_2; (c) HRTEM image; (d) EDS elemental mappings of Pt/Ni-CeO_2 sample.
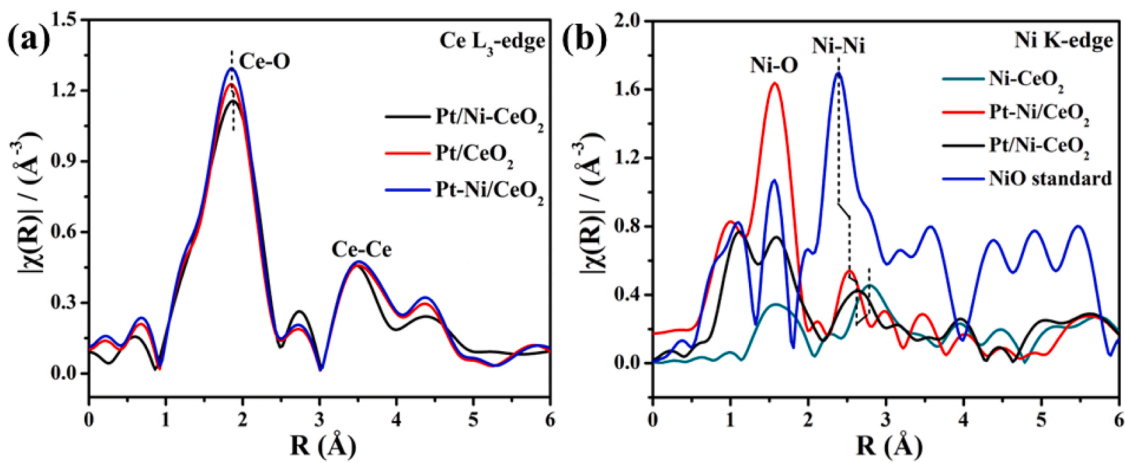
Fig. 3. EXAFS magnitude of the Fourier transformed k^2-weighted $\chi(k)$ data at (a) Ce L$_3$-edge for Pt/Ni-CeO_2, Pt/CeO_2 and Pt-Ni/CeO_2 samples; (b) Ni K-edge for Ni-CeO_2, Pt/Ni-CeO_2, Pt-Ni/CeO_2, and NiO standard samples.
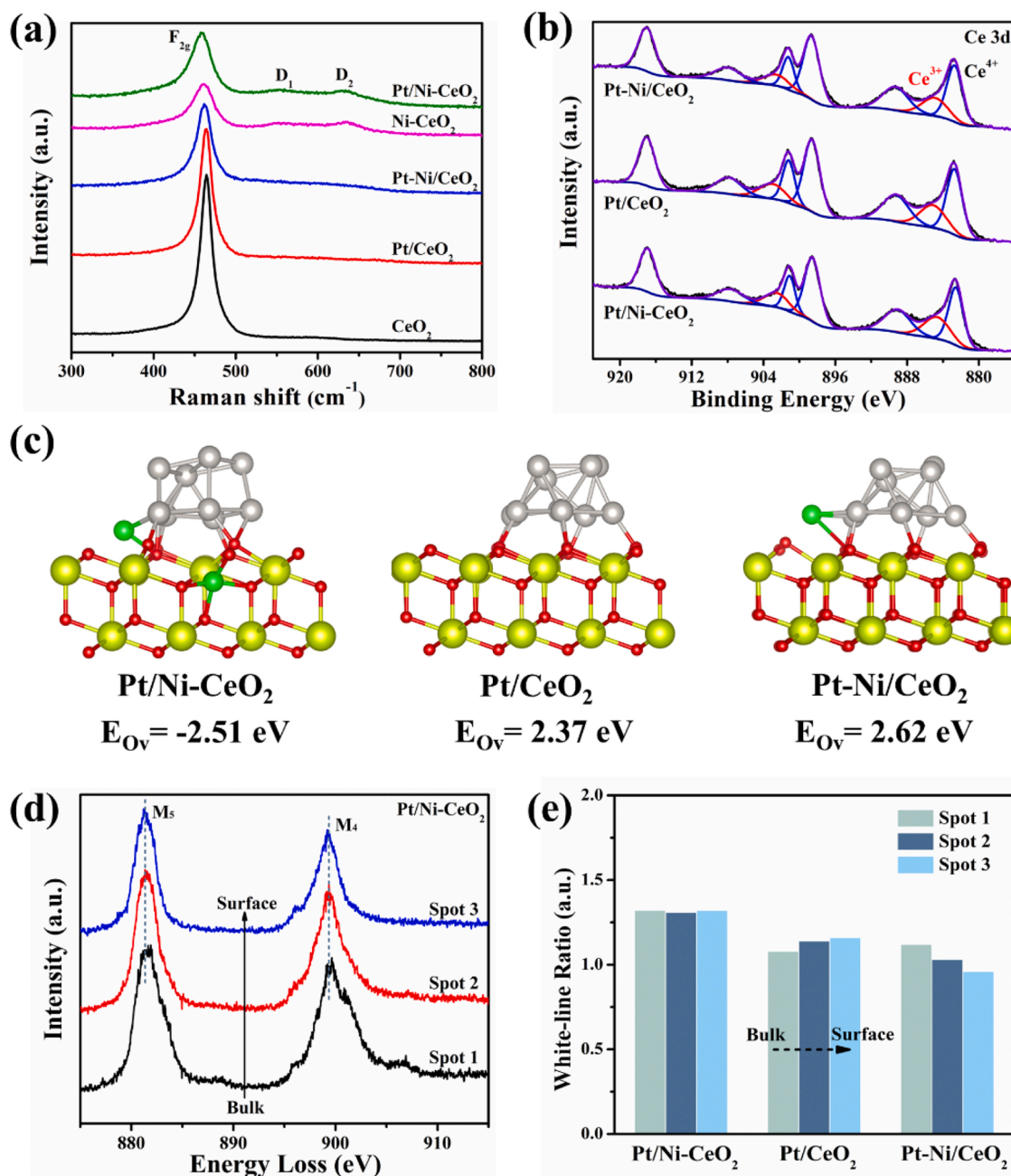
Fig. 4. (a) Raman spectra for the supports and catalysts. (b) Ce 3d XPS spectra. (c) DFT calculation of oxygen vacancy formation energy on as-prepared catalysts (Red, yellow, green, and gray balls represent the oxygen atoms, cerium atoms, nickel atoms, and platinum atoms, respectively). (d) Ce $M_{4,5}$-edge EELS spectra obtained from the yellow spot in Fig. S6 for the Pt/Ni-CeO$_2$ sample. (e) M_5/M_4 white line ratios for all samples.

species, Ni-CeO$_2$ and Pt/Ni-CeO$_2$ samples presented the obvious defect-induced peaks, indicating the formation of abundant oxygen vacancies. The Ce 3d XPS spectra in Fig. 4b could be deconvoluted into eight peaks, in which the peaks at 884.7 and 902.6 eV were attributed to Ce^{3+}, and other peaks were assigned to Ce^{4+}. As shown in Table 1, the percentage of Ce^{3+} follows the order: Pt/Ni-CeO$_2$ (19.1%) > Pt/CeO$_2$ (17.3%) > Pt-Ni/CeO$_2$ (15.9%). The Pt/Ni-CeO$_2$ sample displayed an increased amount of Ce^{3+} species, implying more oxygen vacancies and unsaturated chemical bonds. On the contrary, a spot of Ce^{3+} content was detected in the Pt-Ni/CeO$_2$ sample, revealing the vanishing of some oxygen vacancies by surface Ni species. The XANES spectra of Ce L$_3$-edge (Fig. S8 and Table S2) further verified the XPS results. DFT calculations were used to elucidate the influence of Ni doping on the formation of oxygen vacancy. As described in Fig. 4c, the calculated

energy of oxygen vacancy formation of -2.51 eV in the Pt/Ni-CeO$_2$ sample was lower than those in Pt/CeO$_2$ (2.37 eV) and Pt-Ni/CeO$_2$ (2.62 eV). This result indicated that the doping of Ni species in the Pt/Ni-CeO$_2$ sample was beneficial to the formation of oxygen vacancies, while the surface decoration of Ni species could poison the oxygen vacancies.

To further study the distribution features of Ce^{3+} and oxygen vacancies, the Ce $M_{4,5}$-edge EELS spectra are obtained from the yellow spot in Fig. S9. As shown in Fig. 4d, the EELS spectra of the Pt/Ni-CeO$_2$ sample remained unchanged from bulk to the surface. The M_5 and M_4 edges of the Pt/CeO$_2$ sample (Fig. S10a) successively shifted to lower energy loss, while Pt-Ni/CeO$_2$ (Fig. S10b) exhibited a gradual shift to higher energy loss for M_5 and M_4 edges. The low energy loss represents low valence state elements, so that the as-prepared catalysts exhibited

different Ce^{3+} distribution. According to the white line ratios of M$_5$/M$_4$, the proportion of Ce^{3+} was calculated to investigate the Ce^{3+} distribution [28]. As shown in Fig. 4e, an unchanged and plentiful Ce^{3+} was presented in the Pt/Ni-CeO$_2$ sample, indicating the abundant oxygen vacancies regardless of bulk or surface, while the Pt/CeO$_2$ sample exhibited an increased amount of Ce^{3+} from bulk to surface. Hence, the doping of Ni species in the Pt/Ni-CeO$_2$ sample would facilitate the generation of oxygen vacancies in the CeO$_2$ entirety to enhance the migration and activation ability of oxygen species [33]. On the contrary, more Ce^{3+} existed in the bulk rather than on the surface of the Pt-Ni/-CeO$_2$ sample. This might be the result that the surface NiO in the Pt-Ni/CeO$_2$ sample was deposited around electron-rich Ce^{3+} via electrostatic attraction, rather than electron-deficient Ce^{4+}, thus leading to the annihilation of oxygen vacancies. This is consistent with the DFT calculations results.

Pt 4f spectra in Fig. 5a show six well-fitted peaks with the binding energies of 71.0, 72.5, 73.7, 74.4, 75.8, 77.4 eV, which were assigned to Pt^0 4f$_{7/2}$, Pt^{2+} 4f$_{7/2}$, Pt^0 4f$_{5/2}$, Pt^{4+} 4f$_{7/2}$, Pt^{2+} 4f$_{5/2}$, Pt^{4+} 4f$_{5/2}$, respectively [34]. The quantitative results (Table 1) revealed that the Pt/Ni-CeO$_2$ catalyst possessed the highest Pt^0/Pt$_{total}$ (22.9%) value, followed by Pt/CeO$_2$ (18.6%) and Pt-Ni/CeO$_2$ (15.4%) catalysts. The DRIFT spectra of CO (Fig. S11) also confirmed the more metallic state Pt^0 species on the surface of Pt/Ni-CeO$_2$ catalyst [35]. As previously reported, the metallic state Pt was generally identified as the catalytically active sites for toluene combustion [36,37]. The electrophilic O$_2$ molecules were activated by picking up the electrons from electron-rich Pt species to form nucleophilic oxygen species, which could react with toluene and replenish the consumed lattice oxygen. In Fig. 5b, the asymmetrical O 1s spectra could be divided into three peaks at 529.5,

531.7, and 533.7 eV, corresponding to lattice oxygen species O^{2-} (O$_{latt}$), surface-adsorbed oxygen species O$_2^-$ (O$_{ads}$), and hydroxyl groups (O$_{OH}$), respectively [38]. As shown in Table 1, the O$_{ads}$/O$_{total}$ ratios exhibited the following sequence: Pt/Ni-CeO$_2$ (40.5%) > Pt-Ni/CeO$_2$ (36.2%) > Pt/CeO$_2$ (22.0%), suggesting that the Pt/Ni-CeO$_2$ sample could provide sufficient electrophilic O$_{ads}$ to participate in the oxidation reaction.

H$_2$-TPR were conducted to study redox properties of catalysts. As shown in Fig. S12, the doping of Ni in the Ni-CeO$_2$ support obviously decreased the reduction temperature of oxygen species compared with the CeO$_2$ support. For the Pt/CeO$_2$ sample, the H$_2$-TPR spectra in Fig. 5c showed three obvious peaks, including the reduction of PtO$_x$ and adsorbed active oxygen adjacent to the Pt-CeO$_2$ interface (60–200 °C), surface lattice oxygen (200–400 °C), and bulk lattice oxygen in ceria (above 500 °C). The formation of metallic Pt particles at low temperatures provokes the shift of surface lattice oxygen reduction towards the low-temperature range due to the spillover effect [39]. After the incorporation of Ni species, a new peak at ca. 220 °C was presented on the H$_2$-TPR spectra of Pt-Ni/CeO$_2$ and Pt/Ni-CeO$_2$ samples, which could be assigned to the reduction of surface NiO [40]. The Pt/Ni-CeO$_2$ sample possessed a lower reduction temperature of NiO than the Pt-Ni/CeO$_2$ sample, probably resulting from the higher dispersion of NiO on the catalyst surface and the weak bond with the Ni-CeO$_2$ support [41]. This is consistent with the result of HRTEM. The fitted peak in the Pt-Ni/CeO$_2$ sample revealed that the reduction peaks of adsorbed active oxygen and surface lattice oxygen shifted to higher temperature, indicating a worse low temperature reducibility [42]. The O$_2$-TPD profiles in Fig. 5d can be recognized as three parts, which were attributed to surface active oxygen (60–200 °C), surface lattice oxygen (200–450 °C) and bulk lattice oxygen (above 450 °C). A desorption peak of surface-active oxygen was
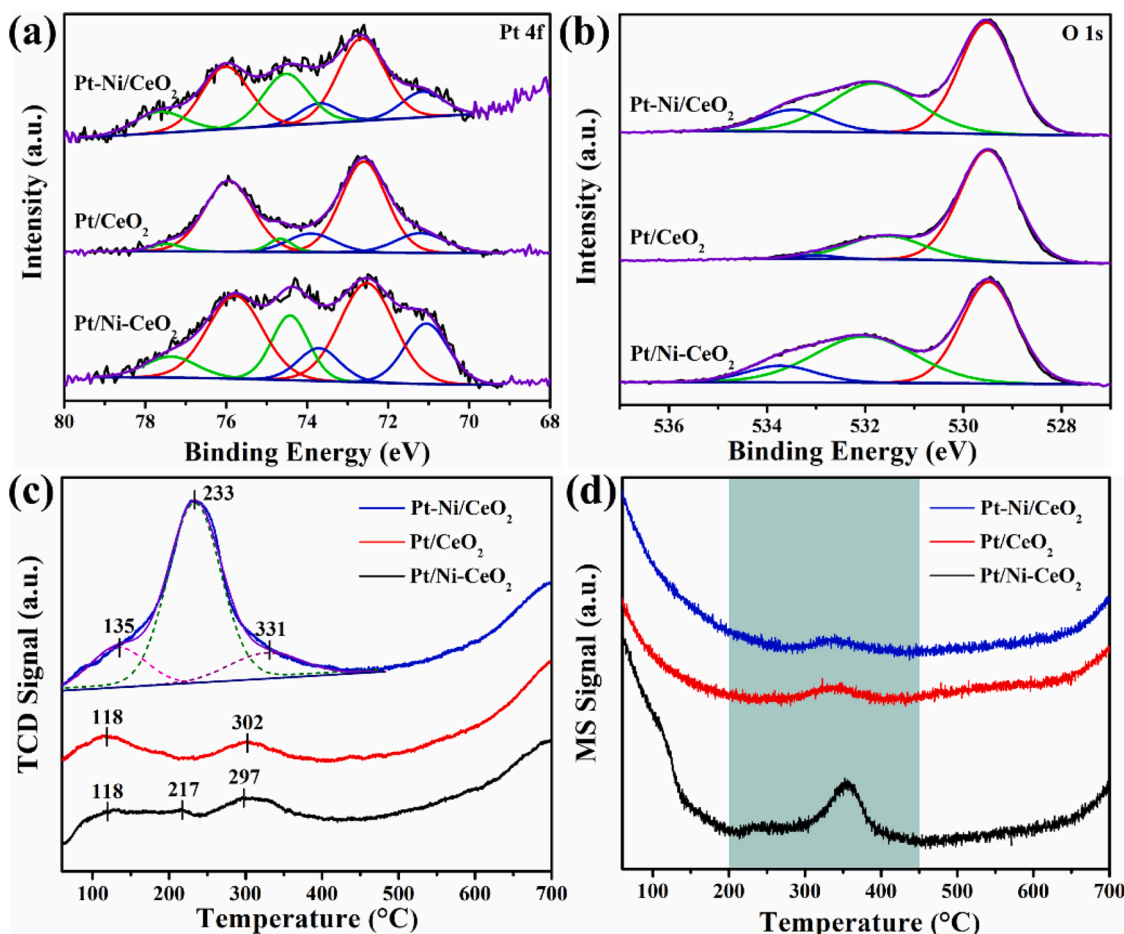

Fig. 5. (a) Pt 4 f; (b) O 1 s XPS spectra. (c) H$_2$-TPR spectra; (d) O$_2$-TPD spectra of as-prepared catalysts.

discerned on the Pt/Ni-CeO$_2$ sample, which could first take part in the oxidation reaction. Meanwhile, the appropriate Ni doping can effectively increase the content of surface lattice oxygen in the Pt/Ni-CeO$_2$ sample, indicating that bulk lattice oxygen could migrate to the surface through bulk oxygen vacancies to boost the desorption of surface oxygen species. These results illustrated that the Pt/Ni-CeO$_2$ sample possessed an excellent redox property.

3.3. Adsorption and activation capacity study

In order to investigate the adsorption and activation ability of reactant molecules, toluene-TPD and oxygen multi-pulse experiment were carried out. As shown in Fig. 6a, a symmetric peak at ca. 100 °C was assigned to the desorption of toluene. A large desorption peak of toluene was observed in the Pt/Ni-CeO$_2$ catalyst, followed by the Pt/CeO$_2$ catalyst, indicating that plentiful toluene could be adsorbed on the surface of the Pt/Ni-CeO$_2$ catalyst. In Fig. 6b, the final product CO$_2$ peaks appeared at 60–230 °C and 300–500 °C, indicating that active oxygen species, including surface adsorbed oxygen and surface lattice oxygen could promote the oxidation reaction behavior of strongly adsorbed toluene. The normalized results of toluene and CO$_2$ by eliminating the influence of specific surface area in Fig. 6c displayed the maximum values in Pt/Ni-CeO$_2$, exhibiting an excellent adsorption and activation capacity of toluene. It is worth noting that the formation of benzene, acetone, acetic acid, and CO were also perceived in Fig. S13 and Fig. 6c, demonstrating that a successive oxidation of toluene occurred in toluene-TPD experiment under oxygen-deficient condition. Furthermore, more intermediates were generated in the Pt/Ni-CeO$_2$

catalyst due to abundant active oxygen species, which was prone to reacting with adsorbed toluene molecules at low temperature.

The active oxygen species in catalysts was prerequisite to participate in VOCs oxidation, whereas the replenishment of gaseous oxygen to the consumed oxygen was essential for the sustainable reaction. As shown in Fig. 6d and Table S3, each pulse formation amounts of CO$_2$ had a tendency to a constant function rather than continuous declination, illustrating that the consumed active oxygen species can be fully replenished by gaseous oxygen. In addition, the larger average value in the Pt/Ni-CeO$_2$ catalyst (Table S3) described the excellent supplementary capacity of oxygen species. An important corollary of this result was that the Pt/Ni-CeO$_2$ catalyst had the abundant oxygen vacancy to fast replenish the consumed active oxygen species by dissociating gaseous oxygen.

3.4. Toluene combustion performance

The toluene catalytic combustion performances over as-prepared catalysts were evaluated under the condition of 1000 ppm toluene, WHSV at 60,000 mL/(g·h) and 5.0 vol% vapor. As displayed in Fig. 7a, the Pt/CeO$_2$ catalyst showed 50% and 90% conversion temperature (T$_{50}$ and T$_{90}$) at 161 and 165 °C (Table S4), respectively, under the feed with 5.0 vol% H$_2$O. After Ni doping, the Pt/Ni-CeO$_2$ catalyst exhibited an excellent performance on toluene combustion, and the T$_{50}$ and T$_{90}$ decreased to 147 and 149 °C, respectively. In contrast, after Ni loading, the catalytic activity over the Pt-Ni/CeO$_2$ catalyst could be suppressed with 166 °C of T$_{50}$ and 170 °C of T$_{90}$. Compared with the catalytic activity without H$_2$O, all the catalysts exhibited the slightly inferior catalytic activity in the presence of H$_2$O. Meanwhile, the catalytic activity
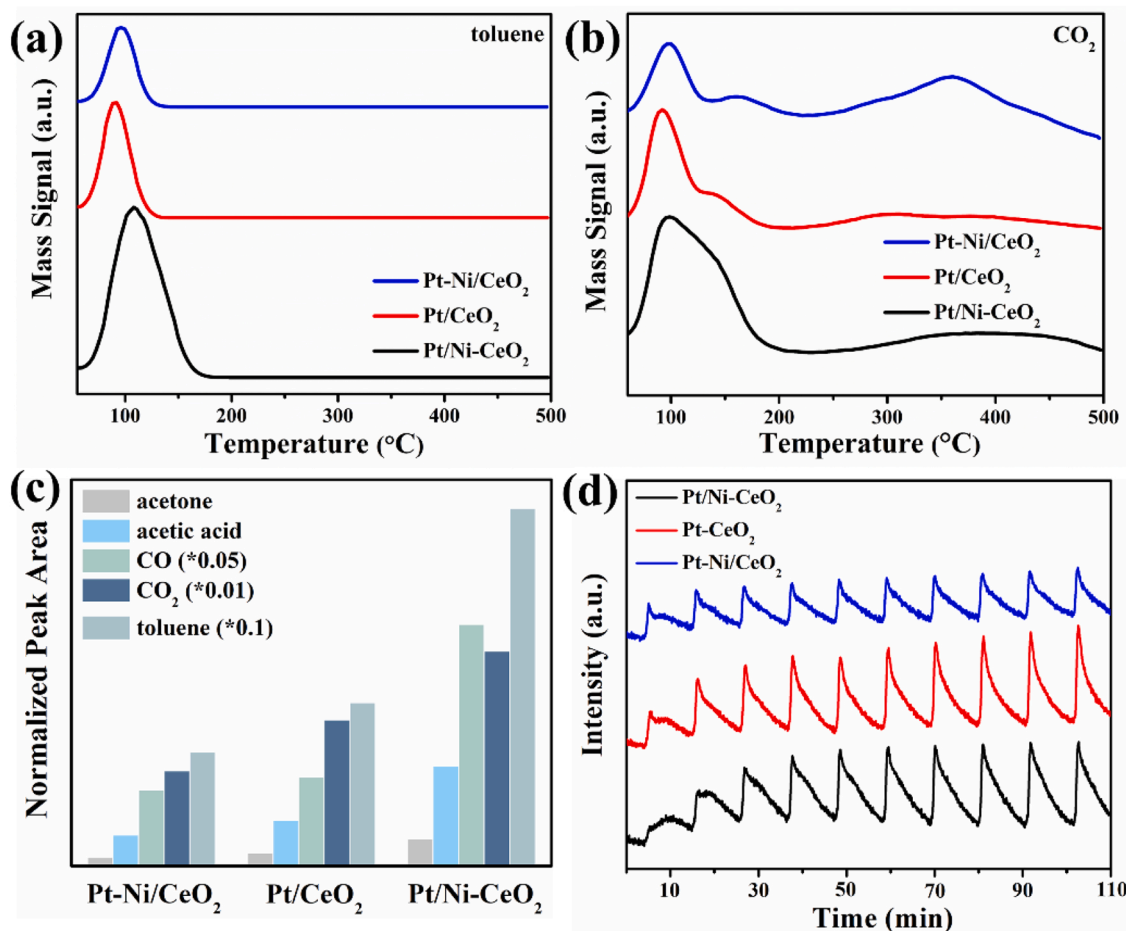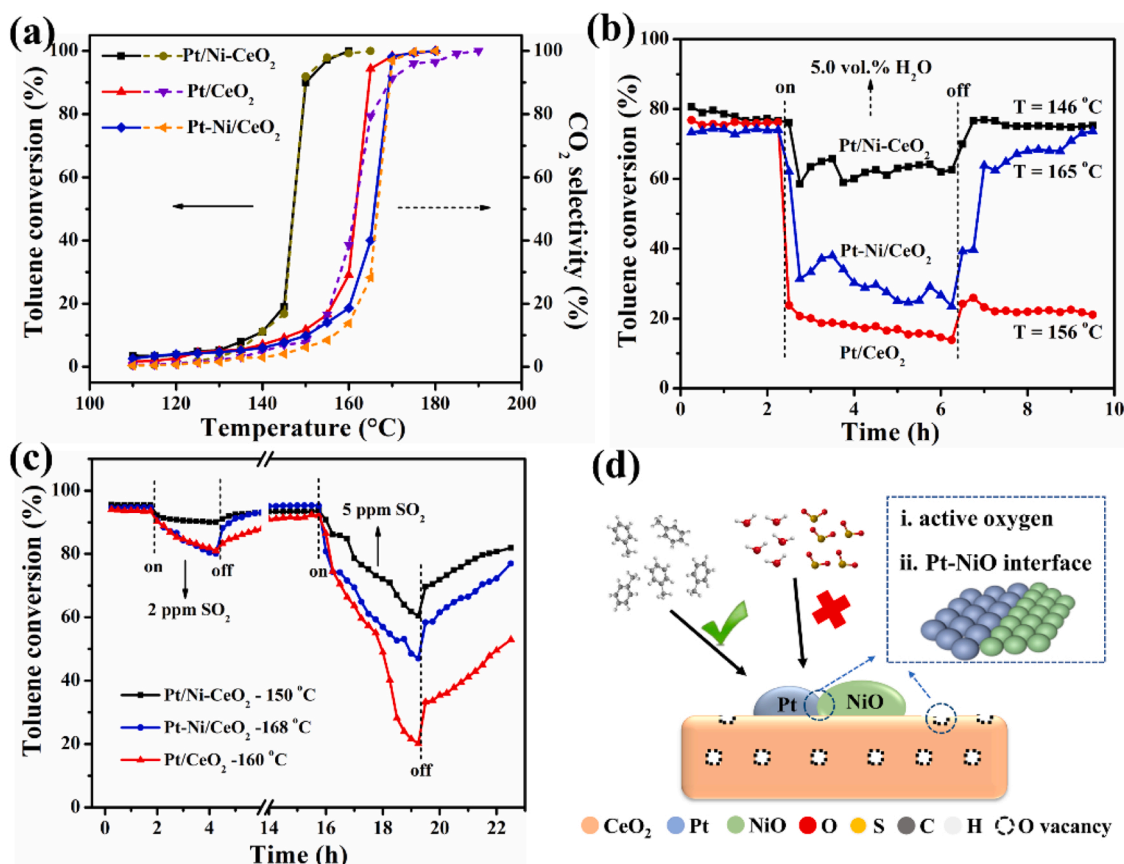

Fig. 6. (a, b) Toluene-TPD profiles of all as-prepared catalysts; (c) The amount of toluene, intermediates and CO$_2$ products (in low temperature range of 60–230 °C) normalized by catalysts surface area from toluene-TPD; (d) CO$_2$ product in oxygen multi-pulse experiment.

Fig. 7. (a) Toluene conversion with 5.0 vol% vapor over as-prepared catalysts as a function of temperature; (b) Effect of the humidity on catalytic stability test for toluene oxidation; (c) The effect of SO_2 poison-resistant on toluene oxidation over as-prepared catalysts; (d) Illustration of water-resistance and SO_2-tolerance mechanism on Pt/Ni-CeO$_2$ catalyst.

of Ni-CeO$_2$ support was lower than that of CeO$_2$ support under the condition without H$_2$O (Fig. S14 and Table S4), which should be related to the doping of Ni ions into the ceria lattice, leading to the loss of surface lattice oxygen [43]. The CO$_2$ selectivity of as-prepared catalysts showed the same increasing trend during the reaction process (Fig. 7a). The Arrhenius plots of the samples were presented in Fig. S15. As shown in Table S4, the *Ea* values increased in the order of Pt/Ni-CeO$_2$ (77.0 kJ/mol) < Pt/CeO$_2$ (104.0 kJ/mol) < Pt-Ni/CeO$_2$ (114.7 kJ/mol), which was consistent with the toluene catalytic activity. The turnover frequency (TOF) was calculated according to the dispersion of Pt. The TOF of Pt/Ni-CeO$_2$ (3.70×10^{-3} s^{-1}) was higher than that of Pt/CeO$_2$ (2.69×10^{-3} s^{-1}), followed by that of Pt-Ni/CeO$_2$ catalyst (2.07×10^{-3} s^{-1}). Compared with the reported literature (Table S5 and Table S6), Pt/Ni-CeO$_2$ exhibited lower conversion temperature of toluene oxidation and a higher TOF value, indicating an excellent intrinsic activity of the Pt/Ni-CeO$_2$ catalyst.

The stability in high humidity was an important factor to influence the practical application for toluene degradation. The water-tolerance on as-prepared catalysts in Fig. 7b exhibited that when the water vapor was introduced, the toluene conversion on as-prepared catalyst all presented a downward trend. An obvious drop was observed on Pt/CeO$_2$ and Pt-Ni/CeO$_2$ catalysts, in which the conversion had decreased below 40%. For the Pt/Ni-CeO$_2$ catalyst, the conversion had a relatively slight decline. Additionally, the toluene conversion could be quickly recovered and kept constant after removal of the water vapor in the Pt/Ni-CeO$_2$ catalyst. Therefore, the Pt/Ni-CeO$_2$ catalyst had a good stability and tolerance to humidity.

Given that the actual emission conditions may contain slight SO$_2$ gas, the influence of SO$_2$ on toluene combustion performance was investigated. As shown in Fig. 7c, the catalytic activity of all as-prepared

catalysts presented a descending trend after SO$_2$ inlet, revealing sulfur-poisoning effect on catalysts. SO$_2$ with strong electronegativity could induce the electron transfer to decrease the electron cloud density of the Pt d-orbital, thus restraining the adsorption of VOCs [44]. Moreover, the surface active sites were often occupied by the formed metallic sulfates and sulfites to cause an irreversible inactivation [45]. When introducing 2 ppm SO$_2$, the toluene conversion decreased slightly and gradually remained unchanged for the Pt/Ni-CeO$_2$ catalyst, which obtained a dynamic equilibrium between the formation and decomposition of sulfates or sulfites on the catalyst surface. The degradation performance over Pt-Ni/CeO$_2$ and Pt/CeO$_2$ catalysts displayed similar decreasing trend with 2 ppm SO$_2$. After adding 5 ppm SO$_2$ into the reaction, the Pt/Ni-CeO$_2$ catalyst showed a preferable sulfur-resistance performance compared with other two catalysts. It was interesting to note that the catalytic activity on the Pt-Ni/CeO$_2$ catalyst decreased more slowly than that of the Pt/CeO$_2$ catalyst, implying that the incorporation of Ni enhanced the sulfur-resistance capacity, in spite of a poor performance on toluene degradation. After cutting off SO$_2$, the toluene conversion could gradually recover, of which the Pt/Ni-CeO$_2$ catalyst exhibited the superior recovery.

Fig. 7d illustrates the water-resistance and SO$_2$-tolerance mechanism on the Pt/Ni-CeO$_2$ catalyst. In the toluene degradation reaction, there was a competitive adsorption between reactant and toxic molecules in the presence of H$_2$O or SO$_2$, easily resulting in the decreased catalytic activity. As confirmed by aforementioned characterizations, the Pt-NiO interfacial structure was formed by the thermal-driven Ni species into the adjacent Pt species, which could modify the electronic and chemical properties of Pt species. The electronic modification was conducive to the surface Pt d-band lower in energy and broader in width, which could reduce the adsorption energy of small molecules [9]. Correspondingly,

the Pt atom at Pt-NiO interface in the Pt/Ni-CeO$_2$ catalyst reduced the possibility of interaction with SO$_2$/OH⁻, thus protecting the active sites from sulfur/H$_2$O poisoning. The abundant oxygen vacancies guaranteed the sufficient active oxygen species to expel the surface sulfur/H$_2$O to some extent once cutting off SO$_2$/H$_2$O, and that led to a gradual recovery of toluene conversion [46,47].

3.5. Degradation mechanism study

In situ DRIFT was performed to investigate the toluene degradation mechanism and how the oxygen vacancies accelerate the oxidation reaction. As shown in Fig. 8a, the peak around 1595 cm^{-1} attributed to the in-plane skeletal vibration of benzene ring indicated the adsorption of toluene molecules [48,49]. The peaks at 1028, 1051, 1104 and 1173 cm^{-1} were assigned to the benzyl alcohol species due to the preliminary oxidation of methyl. The peak at 1445 cm^{-1} was related to the vibration of the skeleton C-C bond derived from the benzene ring of benzaldehyde, while the peaks at 1653 and 1698 cm^{-1} were associated with the C-O vibration peak of benzaldehyde [50,51]. The vibration peaks of benzoate were observed at 1398, 1499 and 1565 cm^{-1}. The formation of maleic anhydride was denoted at 1240, 1309, 1814, 1869 and 1959 cm^{-1}, primarily coming from the opening of benzene ring, namely a deep oxidation. In Fig. 8b and Fig. 8c, the main intermediates were also observed on the surface of Pt/CeO$_2$ and Pt-Ni/CeO$_2$ catalysts, except for the lower peak intensity, demonstrating that both toluene chemical adsorption and further oxidation were significantly boosted in the Pt/Ni-CeO$_2$ catalyst.

According to previous reports, toluene oxidation sequentially produced benzyl alcohol, benzaldehyde, benzoate and maleic anhydride [36,52]. The in situ DRIFTS spectra obviously exhibited the differences of intermediate species as time goes by. In the initial stage, benzyl alcohol and benzaldehyde were dominant until 20 min in the Pt-Ni/-CeO$_2$ sample, while benzaldehyde and benzoate by further oxidation of benzyl alcohol were predominant in the Pt/CeO$_2$ sample, revealing the lack of active oxygen species in the Pt-Ni/CeO$_2$ sample. This was attributed to the annihilation of surface oxygen vacancies by Ni loading. After 30 min, benzyl alcohol was accumulated on the surface of the Pt-Ni/CeO$_2$ sample, and the amount of benzoate was nearly kept constant in the Pt/CeO$_2$ sample, indicating that Pt-Ni/CeO$_2$ and Pt/CeO$_2$ samples had no sufficient active oxygen species to promote the deep toluene oxidation into maleic anhydride. On the contrary, abundant benzoate and maleic anhydride were detected in the Pt/Ni-CeO$_2$ catalyst in the entire process, which demonstrated that the ample active oxygen species promoted a deep oxidation of intermediates and accelerated the rate-determining step among the steps of toluene oxidation. The efficient replenishment of surface-active oxygen by adsorbed oxygen species played the key role in aromatic ring-opening reactions.

Based on the above discussion, the toluene oxidation mechanism and participation pathway of oxygen species were illustrated in Fig. 9.

Toluene first reacted with the adsorbed active oxygen to generate benzaldehyde, benzyl alcohol, and benzoic acid, which derived from the attack of oxygen species on the benzyl group. Abundant oxygen vacancies were formed on the Pt/Ni-CeO$_2$ catalyst from bulk to the surface due to the doping of Ni species. The gaseous O$_2$ molecules could be activated via surface oxygen vacancy and the lattice oxygen could migrate via bulk oxygen vacancy to replenish the consumed active oxygen. Maleic anhydride was the important intermediate after the ring-opening, which is usually the rate-determining step among most oxidation processes of toluene. The efficient replenishment on consumed active oxygen could promote the ring-opening reaction of benzoate into maleic anhydride. The sustainable oxygen replenishment guaranteed the further oxidation of toluene.

4. Conclusions

In this work, Pt/Ni-CeO$_2$ and Pt-Ni/CeO$_2$ catalysts were prepared via the doping or surface decoration of Ni species, and Pt/CeO$_2$ was synthesized by impregnation of Pt. The catalysts were used for catalytic oxidation of toluene. The doping of Ni species in the Pt/Ni-CeO$_2$ catalyst simultaneously promoted the formation of abundant oxygen vacancies from the bulk to the surface. Various characterization results illustrated the roles of surface and bulk oxygen vacancies in toluene oxidation reaction, in which the enhanced activation of gaseous oxygen by surface oxygen vacancies and the improved migration ability of lattice oxygen by bulk oxygen vacancies promoted the toluene catalytic oxidation performance. Thus, the Pt/Ni-CeO$_2$ catalyst exhibited a high TOF value in high humidity at a WHSV of 60,000 mL/(g·h). The formed Pt-NiO interfacial structure by the thermal-driven Ni species to the adjacent Pt species could effectively modify the electronic and chemical properties of Pt species, which suppress the adsorption of water and SO$_2$ molecules. The Pt/Ni-CeO$_2$ catalyst exhibited superior water-resistance, and SO$_2$-tolerance. This work may provide new insights into oxygen vacancies in pollutant removal as well as a strategy of surface modification engineering for catalyst development in practical applications.

CRediT authorship contribution statement

Menglan Xiao: Conceptualization, Methodology, Investigation, Writing – original draft. **Dawei Han**: Data curation, Writing – original draft. **Xueqin Yang**: Visualization, Investigation, Writing – original draft. **Narcisse Tsona Tchinda**: Writing – review & editing. **Lin Du**: Writing – review & editing. **Yucong Guo**: Project administration, Writing – review & editing. **Yuechang Wei**: Methodology, Writing – review & editing. **Xiaolin Yu**: Supervision, Methodology, Writing – review & editing, Funding acquisition. **Maofa Ge**: Supervision, Methodology, Writing – review & editing.
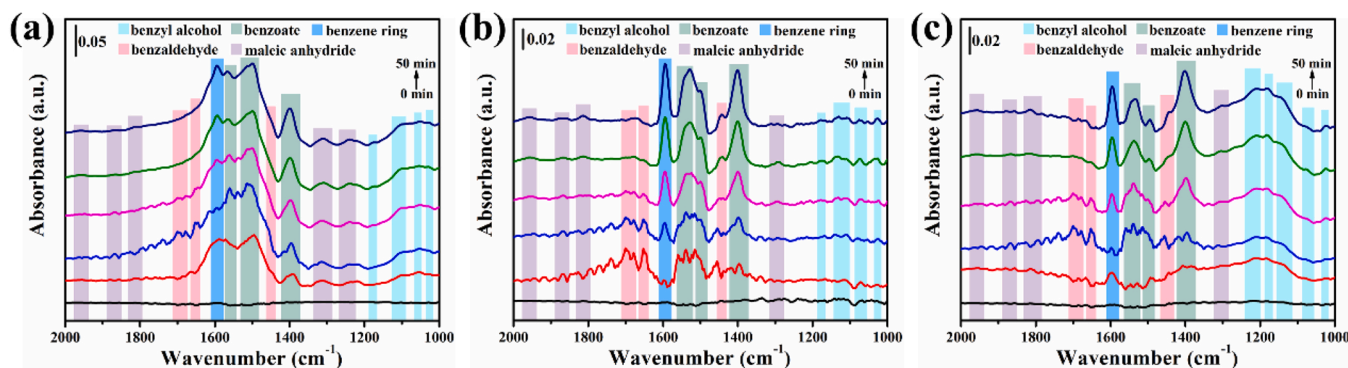

Fig. 8. *In situ* DRIFTS spectra of toluene oxidation as a function of time at 150 °C (Reaction condition: 1000 ppm toluene + 20% O$_2$ + N$_2$ balanced). (a) Pt/Ni-CeO$_2$ catalyst; (b) Pt/CeO$_2$ catalyst; (c) Pt-Ni/CeO$_2$ catalyst.
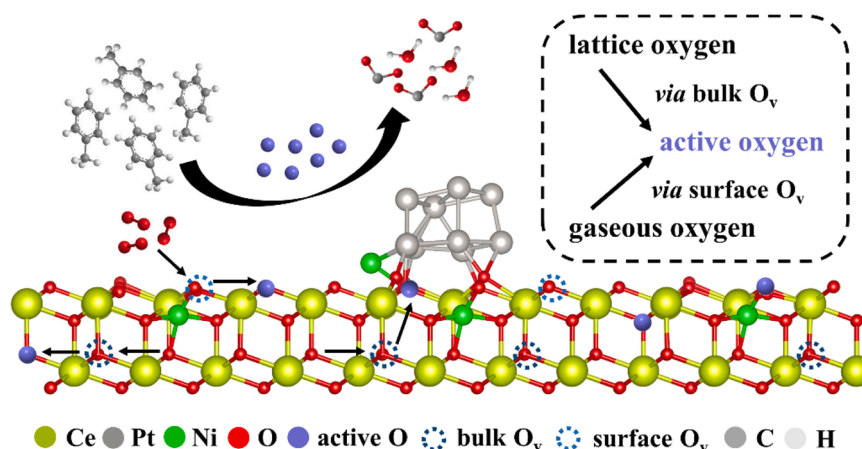
Fig. 9. Illustration of the participation pathway of oxygen species in the process of the toluene oxidation reaction on the Pt/Ni-CeO$_2$ catalyst.

Declaration of Competing Interest

The authors declare that they have no known competing financial interests or personal relationships that could have appeared to influence the work reported in this paper.

Data availability

No data was used for the research described in the article.

Acknowledgements

Appendix A. Supporting information

Supplementary data associated with this article can be found in the online version at doi:10.1016/j.apcatb.2022.122173.

References

[1] M.A. Salaev, A.A. Salaeva, T.S. Kharlamova, G.V. Mamontov, Pt–CeO$_2$-based composites in environmental catalysis: a review, Appl. Catal. B Environ. 295 (2021), 120286.

[2] G. Rochard, L. Olivet, M. Tannous, C. Poupin, S. Siffert, R. Cousin, Recent advances in the catalytic treatment of volatile organic compounds: a review based on the mixture effect, Catalysts 11 (2021) 1218.

[3] Y. Wang, C. Wang, K. Zeng, S. Wang, H. Zhang, X. Li, Z. Wang, C. Zhang, Revealing the strong interaction effect of MnO$_x$ nanoparticles and Nb$_2$O$_5$ supports with variable morphologies on catalytic propane oxidation, Appl. Surf. Sci. 576 (2022), 151797.

[4] J.F. Chen, Y. Yang, S.H. Zhao, F.K. Bi, L. Song, N. Liu, J.C. Xu, Y.X. Wang, X. D. Zhang, Stable black phosphorus encapsulation in porous mesh-like UiO-66 promoted charge transfer for photocatalytic oxidation of toluene and o-dichlorobenzene: performance, degradation pathway, and mechanism, ACS Catal. (2022) 8069–8081.

[5] X.Q. Yang, X.L. Yu, M.Z. Jing, W.Y. Song, J. Liu, M.F. Ge, Defective Mn$_x$Zr$_{1-x}$O$_2$ solid solution for the catalytic oxidation of toluene: insights into the oxygen vacancy contribution, ACS Appl. Mater. Interfaces 11 (2019) 730–739.

[6] M.L. Xiao, X.Q. Yang, Y. Peng, Y.C. Guo, Y.C. Wei, M.F. Ge, X.L. Yu, Confining shell-sandwiched Ag clusters in MnO$_2$-CeO$_2$ hollow spheres to boost activity and stability of toluene combustion, Nano Res. 15 (2022) 7042–7051.

[7] B.-S. Kim, J. Bae, H. Jeong, C. Choe, H. Lee, Surface restructuring of supported nano-ceria for improving sulfur resistance, ACS Catal. (2021) 7154–7159.

[8] M.S. Wilburn, W.S. Epling, SO$_2$ adsorption and desorption characteristics of Pd and Pt catalysts: precious metal crystallite size dependence, Appl. Catal. A Gen. 534 (2017) 85–93.

[9] J.R. Kitchin, J.K. Norskov, M.A. Barteau, J.G. Chen, Modification of the surface electronic and chemical properties of Pt(111) by subsurface 3d transition metals, J. Chem. Phys. 120 (2004) 10240–10246.

[10] S.F. Song, Y.J. Wu, S.S. Ge, L. Wang, Y.S. Wang, Y.L. Guo, W.C. Zhan, Y. Guo, A facile way to improve Pt atom efficiency for CO oxidation at low temperature: modification by transition metal oxides, ACS Catal. 9 (2019) 6177–6187.

[11] Y. Gu, S. Shao, W. Sun, H. Xia, X. Gao, Q. Dai, W. Zhan, X. Wang, The oxidation of chlorinated organic compounds over W-modified Pt/CeO$_2$ catalysts, J. Catal. 380 (2019) 375–386.

[12] L. Kang, L. Han, P. Wang, C. Feng, J. Zhang, T. Yan, J. Deng, L. Shi, D. Zhang, SO$_2$-tolerant NO$_x$ reduction by marvelously suppressing SO$_2$ adsorption over Fe$_\delta$Ce$_{1-\delta}$VO$_4$ catalysts, Environ. Sci. Technol. 54 (2020) 14066–14075.

[13] Y. Lyu, J. Xu, Q. Cao, Z. Zhou, W. Hu, X. Liu, Highly efficient removal of toluene over Cu-V oxides modified γ-Al$_2$O$_3$ in the presence of SO$_2$, J. Hazard. Mater. 436 (2022), 129041.

[14] Z. Xie, B. Yan, J.H. Lee, Q. Wu, X. Li, B. Zhao, D. Su, L. Zhang, J.G. Chen, Effects of oxide supports on the CO$_2$ reforming of ethane over Pt-Ni bimetallic catalysts, Appl. Catal. B Environ. 245 (2019) 376–388.

[15] D.G. Araiza, D.G. Arcos, A. Gómez-Cortés, G. Díaz, Dry reforming of methane over Pt-Ni/CeO$_2$ catalysts: effect of the metal composition on the stability, Catal. Today 360 (2021) 46–54.

[16] T. Gan, J. Yang, D. Morris, X. Chu, P. Zhang, W. Zhang, Y. Zou, W. Yan, S.-H. Wei, G. Liu, Electron donation of non-oxide supports boosts O$_2$ activation on nano-platinum catalysts, Nat. Commun. 12 (2021), 2741-2741.

[17] Y. Cui, X. Shao, M. Baldofski, J. Sauer, N. Nilius, H.-J. Freund, Adsorption, activation, and dissociation of oxygen on doped oxides, Angew. Chem. Int. Ed. 52 (2013) 11385–11387.

[18] K. Harada, T. Oishi, S. Hamamoto, T. Ishihara, Lattice oxygen activity in Pr- and La-doped CeO$_2$ for low-temperature soot oxidation, J. Phys. Chem. C 118 (2014) 559–568.

[19] C. Sun, P. Beaunier, V. La Parola, L.F. Liotta, P. Da Costa, Ni/CeO$_2$ nanoparticles promoted by yttrium doping as catalysts for CO$_2$ methanation, ACS Appl. Nano Mater. 3 (2020) 12355–12368.

[20] A. Gupta, U.V. Waghmare, M.S. Hegde, Correlation of oxygen storage capacity and structural distortion in transition-metal-, noble-metal-, and rare-earth-ion-substituted CeO$_2$ from first principles calculation, Chem. Mater. 22 (2010) 5184–5198.

[21] K. Polychronopoulou, A.A. AlKhoori, A.M. Efstathiou, M.A. Jaoude, C. M. Damaskinos, M.A. Baker, A. Almutawa, D.H. Anjum, M.A. Vasiliades, A. Belabbes, L.F. Vega, A.F. Zedan, S.J. Hinder, Design aspects of doped CeO$_2$ for low-temperature catalytic CO oxidation: transient kinetics and DFT approach, ACS Appl. Mater. Interfaces 13 (2021) 22391–22415.

[22] T.S. Kharlamova, M.V. Salina, V.A. Svetlichnyi, M.A. Salaev, A.I. Stadnichenko, G. V. Mamontov, CeO$_2$-supported Pt–Ag bimetallic catalysts for 4-nitrophenol reduction, Catal. Today 384–386 (2022) 12–24.

[23] X. Xu, L. Liu, Y. Tong, X. Fang, J. Xu, D.-e Jiang, X. Wang, Facile Cr^{3+}-doping strategy dramatically promoting Ru/CeO$_2$ for low-temperature CO$_2$ methanation: unraveling the roles of surface oxygen vacancies and hydroxyl groups, ACS Catal. 11 (2021) 5762–5775.

[24] L. Zhang, G. Spezzati, V. Muravev, M.A. Verheijen, B. Zijlstra, I.A.W. Filot, Y.-Q. Su, M.-W. Chang, E.J.M. Hensen, Improved Pd/CeO$_2$ catalysts for low-temperature NO reduction: activation of CeO$_2$ lattice oxygen by Fe doping, ACS Catal. (2021) 5614–5627.

[25] F. Yang, X. Bao, P. Li, X. Wang, G. Cheng, S. Chen, W. Luo, Boosting hydrogen oxidation activity of Ni in alkaline media through oxygen-vacancy-rich CeO$_2$/Ni heterostructures, Angew. Chem. Int. Ed. 58 (2019) 14179–14183.

[26] H.C. Lee, B.M. Kim, C.K. Jeong, R. Toyoshima, H. Kondoh, T. Shimada, K. Mase, B. Mao, Z. Liu, H. Lee, C.-Q. Huang, W.X. Li, P.N. Ross, B.S. Mun, Surface segregation and oxidation of Pt$_3$Ni(111) alloys under oxygen environment, Catal. Today 260 (2016) 3–7.

[27] J. Kim, W.H. Park, W.H. Doh, S.W. Lee, M.C. Noh, J.J. Gallet, F. Bournel, H. Kondoh, K. Mases, Y. Jung, B.S. Mun, J.Y. Park, Adsorbate-driven reactive interfacial Pt-NiO$_{1-x}$ nanostructure formation on the Pt$_3$Ni(111) alloy surface, Sci. Adv. 4 (2018) 3151.

[28] Z. Su, W. Yang, C. Wang, S. Xiong, X. Cao, Y. Peng, W. Si, Y. Weng, M. Xue, J. Li, Roles of oxygen vacancies in the bulk and surface of CeO$_2$ for toluene catalytic combustion, Environ. Sci. Technol. 54 (2020) 12684–12692.

[29] L. Tao, Y. Shi, Y.-C. Huang, R. Chen, Y. Zhang, J. Huo, Y. Zou, G. Yu, J. Luo, C.-L. Dong, S. Wang, Interface engineering of Pt and CeO$_2$ nanorods with unique interaction for methanol oxidation, Nano Energy 53 (2018) 604–612.

[30] J. Wu, J. Gao, S. Lian, J. Li, K. Sun, S. Zhao, Y.D. Kim, Y. Ren, M. Zhang, Q. Liu, Z. Liu, Z. Peng, Engineering the oxygen vacancies enables Ni single-atom catalyst for stable and efficient C-H activation, Appl. Catal. B Environ. 314 (2022) 121516.

[31] N. Becknell, Y. Kang, C. Chen, J. Resasco, N. Kornienko, J. Guo, N.M. Markovic, G. A. Somorjai, V.R. Stamenkovic, P. Yang, Atomic structure of Pt$_3$Ni nanoframe electrocatalysts by in situ X-ray absorption spectroscopy, J. Am. Chem. Soc. 137 (2015) 15817–15824.

[32] H.-X. Liu, S.-Q. Li, W.-W. Wang, W.-Z. Yu, W.-J. Zhang, C. Ma, C.-J. Jia, Partially sintered copper–ceria as excellent catalyst for the high–temperature reverse water gas shift reaction, Nat. Commun. 13 (2022) 867.

[33] Y. Yang, S. Zhao, F. Bi, J. Chen, Y. Li, L. Cui, J. Xu, X. Zhang, Oxygen-vacancy-induced O$_2$ activation and electron-hole migration enhance photothermal catalytic toluene oxidation, Cell Rep. Phys. Sci. 3 (2022), 101011.

[34] Y. Li, P. Zhang, J. Xiong, Y. Wei, H. Chi, Y. Zhang, K. Lai, Z. Zhao, J. Deng, Facilitating catalytic purification of auto-exhaust carbon particles via the Fe$_2$O$_3${113} facet-dependent effect in Pt/Fe$_2$O$_3$ catalysts, Environ. Sci. Technol. 55 (2021) 16153–16162.

[35] H. Jeong, D. Shin, B.-S. Kim, J. Bae, S. Shin, C. Choe, J.W. Han, H. Lee, Controlling oxidation state of Pt single-atoms for maximizing catalytic activity, Angew. Chem. Int. Ed. 59 (2020) 20691–20696.

[36] D. Yan, T. Li, P. Liu, S. Mo, J. Zhong, Q. Ren, Y. Sun, H. Cheng, M. Fu, J. Wu, P. Chen, H. Huang, D. Ye, In-situ atmosphere thermal pyrolysis of spindle-like Ce (OH)CO$_3$ to fabricate Pt/CeO$_2$ catalysts: enhancing Pt-O-Ce bond intensity and boosting toluene degradation, Chemosphere 279 (2021) 130658-130658.

[37] M. Xiao, X. Yu, Y. Guo, M. Ge, Boosting toluene combustion by tuning electronic metal–support interactions in in situ grown Pt@Co$_3$O$_4$ catalysts, Environ. Sci. Technol. 56 (2022) 1376–1385.

[38] C.F. Huang, Y.S. Zhang, X.W. Li, H.J. Cao, Y.M. Guo, C.H. Zhang, Mn-incorporated Co3O4 bifunctional electrocatalysts for zinc-air battery application: an experimental and DFT study, Appl. Catal. B Environ. 319 (2022) 121909.

[39] T.A. Bugrova, T.S. Kharlamova, V.A. Svetlichnyi, A.S. Savel'eva, M.A. Salaev, G. V. Mamontov, Insights into formation of Pt species in Pt/CeO$_2$ catalysts: effect of treatment conditions and metal-support interaction, Catal. Today 375 (2021) 36–47.

[40] V. Golovanova, M.C. Spadaro, J. Arbiol, V. Golovanov, T.T. Rantala, T. Andreu, J. R. Morante, Effects of solar irradiation on thermally driven CO$_2$ methanation using Ni/CeO2–based catalyst, Appl. Catal. B Environ. 291 (2021), 120038.

[41] T.A. Bugrova, G.V. Mamontov, The study of CrO $_{(x)}$ -containing catalysts supported on ZrO$_2$, CeO$_2$, and Ce$_{(x)}$Zr$_{(1-x)}$O$_2$ in Isobutane Dehydrogenation, Kinet. Catal. 59 (2018) 143–149.

[42] J. Xiong, Z.G. Li, P. Zhang, Q. Yu, K.X. Li, Y.L. Zhang, Z. Zhao, J. Liu, J.M. Li, Y. C. Wei, Optimized Pt-MnO$_x$ interface in Pt-MnO$_x$/3DOM-Al$_2$O$_3$ catalysts for enhancing catalytic soot combustion, Chin. Chem. Lett. 32 (2021) 1447–1450.

[43] D. Chen, D. He, J. Lu, L. Zhong, F. Liu, J. Liu, J. Yu, G. Wan, S. He, Y. Luo, Investigation of the role of surface lattice oxygen and bulk lattice oxygen migration of cerium-based oxygen carriers: XPS and designed H$_2$-TPR characterization, Appl. Catal. B Environ. 218 (2017) 249–259.

[44] G.A. Somorjai, On the mechanism of sulfur poisoning of platinum catalysts, J. Catal. 27 (1972) 453–456.

[45] G. Li, K. Shen, P. Wu, Y. Zhang, Y. Hu, R. Xiao, B. Wang, S. Zhang, SO$_2$ Poisoning mechanism of the multi-active center catalyst for chlorobenzene and NO$_x$ synergistic degradation at dry and humid environments, Environ. Sci. Technol. 55 (2021) 13186–13197.

[46] P. Wachter, C. Gaber, J. Raic, M. Demuth, C. Hochenauer, Experimental investigation on H$_2$S and SO$_2$ sulphur poisoning and regeneration of a commercially available Ni-catalyst during methane tri-reforming, Int. J. Hydrog. Energy 46 (2021) 3437–3452.

[47] Y. Li, M.Q. Shen, J.Q. Wang, T.M. Wan, J. Wang, Influence of sulfation and regeneration on Pt/Al$_2$O$_3$ for NO oxidation, Catal. Sci. Technol. 5 (2015) 1731–1740.

[48] Y. Luo, Y. Zheng, J. Zuo, X. Feng, X. Wang, T. Zhang, K. Zhang, L. Jiang, Insights into the high performance of Mn-Co oxides derived from metal-organic frameworks for total toluene oxidation, J. Hazard. Mater. 349 (2018) 119–127.

[49] Z. Wang, P. Ma, K. Zheng, C. Wang, Y. Liu, H. Dai, C. Wang, H.-C. Hsi, J. Deng, Size effect, mutual inhibition and oxidation mechanism of the catalytic removal of a toluene and acetone mixture over TiO$_2$ nanosheet-supported Pt nanocatalysts, Appl. Catal. B Environ. 274 (2020), 118963.

[50] Y.J. Shen, J. Deng, S. Impeng, S.X. Li, T.T. Yan, J.P. Zhang, L.Y. Shi, D.S. Zhang, Boosting toluene combustion by engineering Co-O Strength in cobalt oxide catalysts, Environ. Sci. Technol. 54 (2020) 10342–10350.

[51] X.D. Zhang, F.K. Bi, Z.Y. Zhao, Y. Yang, Y.T. Li, L. Song, N. Liu, J.C. Xu, L.F. Cui, Boosting toluene oxidation by the regulation of Pd species on UiO-66: synergistic effect of Pd species, J. Catal. 413 (2022) 59–75.

[52] D. Han, X. Ma, X. Yang, M. Xiao, H. Sun, L. Ma, X. Yu, M. Ge, Metal organic framework-templated fabrication of exposed surface defect-enriched Co$_3$O$_4$ catalysts for efficient toluene oxidation, J. Colloid Interface Sci. 603 (2021) 695–705.